

Power allocation for cell-free MIMO integrated sensing and communication

Guoqing Xia, Pei Xiao, Qu Luo, Bing Ji, Yue Zhang, Huiyu Zhou

Abstract—In this paper, we investigate integrated sensing and communication (ISAC) in a cell-free (CF) multiple-input multiple-output (MIMO) network with single-antenna access points (APs), where each AP functions either as a transmitter for both sensing and communication or as a receiver for target-reflected signals. We derive closed-form Cramér–Rao lower bounds (CRLBs) for location and velocity estimation under arbitrary power allocation ratios, assuming the radar cross-section (RCS) is deterministic and unknown over the observation interval. A power allocation optimization problem is formulated to maximize the communication signal-to-interference-plus-noise ratio (SINR), subject to CRLB-based sensing constraints and per-transmitter power limits. To solve the resulting nonlinear and non-convex problem, we propose a penalty function and projection-based modified conjugate gradient algorithm with inexact line search (PP-MCG-ILS), and an alternative method based on a modified steepest descent approach (PP-MSD-ILS). Additionally, for power minimization in pure sensing scenarios, we introduce a penalty function-based normalized conjugate gradient algorithm (P-NCG-ILS). We analyze the convergence behavior and qualitatively compare the computational complexity of the proposed algorithms. Simulation results confirm the accuracy of the derived CRLBs and demonstrate the effectiveness of the proposed power allocation strategies in enhancing both sensing and overall ISAC performance.

Index Terms—Cell-free MIMO ISAC, CRLB, Power allocation, Penalty function, Projection operator, Conjugate gradient.

I. INTRODUCTION

INTEGRATED sensing and communication (ISAC) has emerged as a key enabling technology for sixth-generation (6G) applications, such as smart cities, autonomous driving, and remote healthcare [1], [2]. Unlike traditional systems with separate designs for communication and sensing, ISAC unifies these functionalities within shared hardware platforms and spectral resources, thereby significantly enhancing spectral, energy, and hardware efficiency [3], [4].

Depending on the geometric deployment of transmitters and receivers, various ISAC system architectures have been

proposed. In mono-static ISAC systems—where the transmitter and receiver are co-located—advanced beamforming techniques are employed to mitigate self-interference in full-duplex operations [5], [6]. In contrast, cell-free (CF) or multi-static ISAC systems involve widely distributed transmitters and receivers. These systems inherit advantages from both CF communication and distributed multi-static radar due to their architectural similarities [7]. MIMO (multiple-input, multiple-output) technology plays a central role by employing orthogonal waveforms across transmitters to achieve multiplexing and diversity gains for both communication and sensing [8]. Owing to these benefits, CF MIMO-empowered ISAC has been actively explored for unified communication-sensing operations [9]–[14].

ISAC systems address a range of sensing tasks, including target detection [15]–[17], and parameter estimation for radar cross-section (RCS) [18], [19], location [20]–[22], velocity [23], [24], and angle [25], [26]. These capabilities support diverse applications from navigation to environmental monitoring. A fundamental challenge in ISAC system design is the formulation of robust performance metrics, which are critical for resource optimization and balancing communication-sensing trade-offs [3], [4]. While unified metrics based on mutual information [27] and Kullback–Leibler divergence [28] have been proposed, tailoring such metrics to specific sensing objectives remains challenging. Consequently, task-specific metrics for sensing and communication continue to be widely adopted.

For communication, Shannon capacity underpins metrics such as spectral efficiency [29], achievable rate [30], and signal-to-interference-plus-noise ratio (SINR). Other metrics like coverage probability and energy efficiency have also been addressed in scenarios with stringent requirements [31]. On the sensing side, metrics such as sensing mutual information [32], [33], sensing SINR [9], [10], and the Cramér–Rao lower bound (CRLB) [34]–[41] have been explored extensively, with CRLB-based designs proving particularly effective.

CRLB-based approaches fall into two categories depending on the RCS model:

Random RCS assumption: RCS values are treated as random variables, and likelihood functions are derived by averaging over their distributions [34]–[37]. These studies established CRLBs for joint location and velocity estimation, and later extended them to multi-target scenarios.

Deterministic RCS assumption: RCS values are assumed to be deterministic but unknown and spatially diverse [38]–[41]. This model is particularly relevant in slowly varying environments or when prior RCS knowledge is unavailable. Under

This work was supported in part by the U.K. Engineering and Physical Sciences Research Council under Grant EP/X013162/1.

Guoqing Xia and Bing Ji are with the School of Engineering, University of Leicester, LE1 7RH Leicester, UK (e-mail: gx21@leicester.ac.uk; bing.ji@leicester.ac.uk).

Pei Xiao is with 5GIC & 6GIC, Institute for Communication Systems (ICS) of University of Surrey, Guildford, GU2 7XH, UK (e-mail: p.xiao@surrey.ac.uk).

Qu Luo is with Institute for Communication Systems (ICS) of University of Surrey, Guildford, GU2 7XH, UK (e-mail: q.u.luo@surrey.ac.uk).

Yue Zhang is with the Institute for Communication Systems and Measurement of China, Chengdu 610095, China (e-mail: zhangyue@icsmcn.cn).

Huiyu Zhou is with the School of Computing and Mathematical Sciences, University of Leicester, LE1 7RH Leicester, UK (e-mail: hz143@leicester.ac.uk).

this setting, CRLBs for both single-target and multiple-target location estimation have been analyzed, with [39] showing convergence to single-target performance as target separations increase.

However, most of the above CRLB formulations rely on continuous-time signal models, while practical radar systems process discrete-time signals, where the sampling rate significantly impacts sensing accuracy. Our prior work [42] introduces a discrete-time likelihood function over Gaussian channels as a more realistic model. Building on this, we derive CRLBs for joint location and velocity estimation under the deterministic RCS assumption in both single- and multiple-target scenarios.

Another critical challenge lies in resource allocation, involving time [43], frequency [44], [45], space [46], [47], and power [9]–[14]. While recent works have addressed power allocation for maximizing sensing SINR or minimizing power under CRLB and communication constraints [9]–[13], they typically consider localization only, neglecting velocity or angular estimation, and are based on continuous-time models that overlook the impact of sampling rate.

In contrast, this paper focuses on joint location and velocity estimation using discrete-time signal models. Even with simplified CRLBs, the resulting CRLB-constrained power allocation problems are highly nonlinear and non-convex, posing significant challenges to analytical optimization. To address this, we leverage advanced optimization techniques including penalty methods, projection operations, and gradient-based search, building algorithms suitable for such complex constrained problems.

A. Contribution

This paper addresses the power allocation problem in a CF MIMO-ISAC system with widely distributed single-antenna access points (APs), where each AP operates as either an ISAC transmitter or sensing receiver. We derive CRLBs for joint location and velocity estimation using discrete received signals under the deterministic RCS assumption. These CRLBs are adopted as sensing metrics to guide power allocation under communication SINR maximization objectives. The main contributions are as follows.

1) We derive the approximate CRLBs for joint location and velocity estimation of a single target under arbitrary power allocations. The CRLBs are validated against MLE results, confirming their effectiveness as performance metrics. With the sensing requirements constrained by the CRLBs of both location and velocity estimation, we propose a Penalty-function based Normalized Modified Conjugate Gradient algorithm with Inexact Line Search (P-NMCG-ILS) to generate a power allocation scheme for the total power minimization. Simulation results verify its effectiveness.

2) We formulate the CF MIMO-ISAC power allocation problem as a communication SINR maximization task, subject to constraints on both location and velocity CRLBs and total/individual power budgets. To tackle the non-convexity and nonlinearity, we propose a Penalty-function and Projection-based Modified Conjugate Gradient algorithm with Inexact

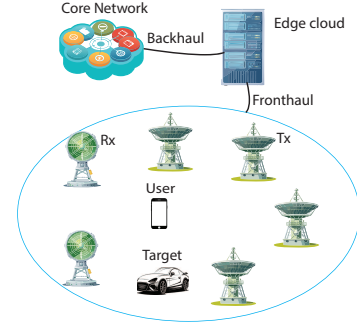


Fig. 1: CF MIMO system for ISAC.

Line Search (PP-MCG-ILS) together with PP-MSD-ILS algorithm based on the modified steepest descent algorithm (MSD).

3) The proposed PA algorithms for sensing and CF MIMO-ISAC can be broadly applicable to constrained non-convex optimization problems involving affine equality constraints (handled via projection) and nonlinear inequality constraints (handled via penalties). We analyze their convergence and computational complexity. Simulation results demonstrate the robust performance, fast convergence, and effectiveness of the proposed algorithms (e.g., PP-MCG-ILS) in optimizing joint sensing and communication performance.

The remainder of the following parts of this paper is organized as follows. Section II describes the received signal model for ISAC. Section IV formulates the power allocation problem for ISAC. Section V details the proposed ISAC power allocation algorithms. Section VII gives the convergence and computational complexity analysis. Section VIII illustrates the simulation results. Section IX concludes this paper.

Notation: \mathbb{R} and \mathbb{C} denote the field of real and complex numbers, respectively. Scalars are denoted by lower-case letters, vectors and matrices respectively by lower- and upper-case boldface letters. The conjugate, transpose and conjugate transpose are denoted by $(\cdot)^*$, $(\cdot)^T$ and $(\cdot)^H$, respectively. $\mathbb{E}\{\cdot\}$ and $|\cdot|$ denote the mathematical expectation and element-wise modulus, respectively. $\text{diag}\{\cdot\}$ generates a diagonal matrix by utilising the input entries as the diagonal elements or diagonal blocks by the given order. $\|\cdot\|$ denotes the l_2 norm of a matrix. The notations $\min\{\cdot\}$ and $\max\{\cdot\}$ denote the minimum and maximum element of the enclosed set $\{\cdot\}$, respectively.

II. SIGNAL MODEL

As shown in Fig. 1, we consider a CF MIMO-ISAC system with widely separated APs. Each AP either serves as an ISAC transmitter or a sensing receiver, similar to the setup in [9], [10]. Assume there are N single-antenna transmitters and K single-antenna receivers, with the positions of the transmitter n and receiver k denoted as $\mathbf{l}_n = [x_n, y_n]^T$ and $\mathbf{l}_k = [x_k, y_k]^T$, respectively. All transmitters and receivers are scheduled and managed by the edge cloud and the core network, e.g., the fifth generation (5G) communication networks. Denote the location and velocity vectors of the q th sensing target as $\mathbf{l}_q = [x_q, y_q]^T$ and $\mathbf{v}_q = [v_{x,q}, v_{y,q}]^T$, respectively.

The Doppler frequency introduced by the relative radial velocity of target q versus any transmitter n and receiver k , is computed as

$$f_{n,k,q} = \frac{1}{\lambda} \mathbf{v}_q^T \left(\frac{\mathbf{l}_n - \mathbf{l}_q}{\|\mathbf{l}_n - \mathbf{l}_q\|_2} + \frac{\mathbf{l}_k - \mathbf{l}_q}{\|\mathbf{l}_k - \mathbf{l}_q\|_2} \right), \quad (1)$$

where λ denotes the wavelength. Denote $\tau_{n,k,q}$ as the propagation delay between the n th transmitter and the k th receiver, as reflected by the q th target. Then, we have

$$\tau_{n,k,q} = \tau_{n,q} + \tau_{k,q}, \quad (2a)$$

$$\tau_{n,q} = \|\mathbf{l}_n - \mathbf{l}_q\|_2 / c, \quad (2b)$$

$$\tau_{k,q} = \|\mathbf{l}_k - \mathbf{l}_q\|_2 / c, \quad (2c)$$

where $\tau_{n,q}$ and $\tau_{k,q}$ represent the propagation delays from the n th transmitter to the q th target, and from the target to the k th receiver, respectively, and c denotes the speed of light. In this paper, we consider the single-target scenario, and thus the subscript q can be omitted.

A waveform $s_n(t)$, with unit energy $\varepsilon_s = \int |s_n(t)|^2 dt = 1$, is considered for both sensing and communication for the n th transmitter. The baseband transmitted signal at transmitter n is denoted as

$$\mathbf{x}_n(t) = \sqrt{P\rho_n} b_n \varsigma s_n(t), \quad (3)$$

where P denotes the total available energy, ρ_n is the power allocation (PA) factor with $\sum_{n=1}^N \rho_n = 1$, b_n is the normalized transmit beamforming weight with $|b_n|^2 = 1$, and ς is the complex data symbol with $\mathbb{E}\{|\varsigma|^2\} = 1$. Denote $\boldsymbol{\rho} = [\rho_1, \rho_2, \dots, \rho_N]^T$ by the vector of the PA coefficient of the N transmitters.

For target-reflected reception, we refer the term ‘‘RCS’’ as encompassing both channel fading and radar RCS. Then, we define the RCS as $\alpha_{n,k}$ over transmitter n and receiver k . We consider the Swerling-I sensing model, i.e. the *deterministic RCS assumption* where RCSs are assumed to be deterministic but unknown during the observation time [38], [40], [41], [48], [49]. The lowpass equivalent of the reflected signal from the n th transmitter by a target received at receiver k is given by¹

$$r_{n,k}(t) = \alpha_{n,k} y_{n,k}(t) + z_{n,k}(t), \quad (4)$$

where $z_{n,k}(t)$ denotes the clutter-plus-noise and $y_{n,k}(t)$ is the loss-free and noise-free received signal,

$$y_{n,k}(t) = \sqrt{P\rho_n} b_n s_n(t - \tau_{n,k}) e^{j2\pi f_{n,k} t}. \quad (5)$$

Note that clutters can initially be mitigated by Doppler processing or space-time adaptive processing [51] and whitened through a whitening filter [34]. It is reasonable to assume the clutter-plus-noise to be additive white Gaussian noise with zero mean and variance σ_{cn}^2 [8], [34]–[36], [52], [53]. Define $\delta_{cn} = \frac{P}{\tau_{eff} \sigma_{cn}^2}$ as the signal-to-clutter-plus-noise ratio (SCNR).

The received signal of the communication user is given by,

$$r_u(t) = \sqrt{P} \sum_{n=1}^N g_n b_n \sqrt{\rho_n} s_n(t) + z(t), \quad (6)$$

¹The transmitted signals over different transmitters are orthogonal and maintain approximate orthogonality over different delays and Doppler frequencies such that the signals contributed from different transmitters can be separated at each receiver [8], [34]–[36], [50].

where g_n is the channel fading between the transmitter n and the user, and the interference-plus-noise $z(t)$ is assumed to be the additive circular Gaussian white with zero mean and variance σ_z^2 . Then, the SINR at the user terminal can be given by

$$\gamma = \sum_{n=1}^N |g_n b_n|^2 \rho_n \delta \stackrel{(i)}{=} \delta \mathbf{p}^T \mathbf{g} \quad (7)$$

where $\delta = \frac{P}{\tau_{eff} \sigma_z^2}$ is the total SINR and \mathbf{g} denotes the channel gain² with its n th element being $|g_n|^2$. Note that (i) holds when using a normalized conjugate beamforming weight with $b_n = g_n^* / |g_n|$.

III. SENSING METRIC

In this section, we present an approximate CRLB for CF MIMO radar under arbitrary power allocations.

First define the squared effective bandwidth (SEBW) and squared effective pulse time width (SETW) as

$$\bar{f}_n^2 = \frac{1}{4\pi^2} \int \left| \frac{ds_n(t - \tau_{n,k})}{d\tau_{n,k}} \right|^2 dt = \int f^2 |S_n(f)|^2 df, \quad (8)$$

and

$$\bar{t}_n^2 = \int t^2 |s_n(t)|^2 dt, \quad (9)$$

respectively. The cross-term between time and frequency is further defined as

$$\sigma_{tf} = \int t s_n^*(t - \tau_{n,k}) \frac{ds_n(t - \tau_{n,k})}{d\tau_{n,k}} dt. \quad (10)$$

We further define the average frequency as

$$\bar{f}_n = \int f |S_n(f)|^2 df, \quad (11)$$

and average time as

$$\bar{t}_n = \int t |s_n(t)|^2 dt. \quad (12)$$

With a relatively large bandwidth and pulse time width, such that $\bar{f}_n^2 \ll \bar{f}_n^2$ and $(\bar{t}_n + \tau_{n,k})^2 \ll \bar{t}_n^2$, we have derived the approximate CRLBs for both location and velocity [42], respectively given by

$$\mathbf{C}_L = (\mathbf{P} - \mathbf{V}\mathbf{Y}^{-1}\mathbf{V}^T)^{-1}, \quad (13)$$

and

$$\mathbf{C}_V = (\mathbf{Y} - \mathbf{V}^T \mathbf{P}^{-1} \mathbf{V})^{-1}. \quad (14)$$

The corresponding 2×2 sub-matrix \mathbf{P} is given in (15), \mathbf{V} given in (16), and

$$\mathbf{Y} = \sum_{n=1}^N \sum_{k=1}^K \begin{bmatrix} \xi_{n,k}^2 d_{n,k} & \xi_{n,k} \varrho_{n,k} d_{n,k} \\ \varrho_{n,k} \xi_{n,k} d_{n,k} & \varrho_{n,k}^2 d_{n,k} \end{bmatrix}. \quad (17)$$

²The communication channels are assumed to be estimated a priori using pilot signals [9]–[13].

$$\mathbf{P} = \sum_{n=1}^N \sum_{k=1}^K \begin{bmatrix} \beta_{n,k}^2 a_{n,k} + 2\beta_{n,k}\eta_{n,k}b_{n,k} + \eta_{n,k}^2 d_{n,k} & \beta_{n,k}\zeta_{n,k}a_{n,k} + (\beta_{n,k}\kappa_{n,k} + \zeta_{n,k}\eta_{n,k})b_{n,k} + \eta_{n,k}\kappa_{n,k}d_{n,k} \\ \zeta_{n,k}\beta_{n,k}a_{n,k} + (\zeta_{n,k}\eta_{n,k} + \beta_{n,k}\kappa_{n,k})b_{n,k} + \kappa_{n,k}\eta_{n,k}d_{n,k} & \zeta_{n,k}^2 a_{n,k} + 2\zeta_{n,k}\kappa_{n,k}b_{n,k} + \kappa_{n,k}^2 d_{n,k} \end{bmatrix}, \quad (15)$$

$$\mathbf{V} = \sum_{n=1}^N \sum_{k=1}^K \begin{bmatrix} \beta_{n,k}\xi_{n,k}b_{n,k} + \eta_{n,k}\xi_{n,k}d_{n,k} & \beta_{n,k}\varrho_{n,k}b_{n,k} + \eta_{n,k}\varrho_{n,k}d_{n,k} \\ \zeta_{n,k}\xi_{n,k}b_{n,k} + \kappa_{n,k}\xi_{n,k}d_{n,k} & \zeta_{n,k}\varrho_{n,k}b_{n,k} + \kappa_{n,k}\varrho_{n,k}d_{n,k} \end{bmatrix}, \quad (16)$$

The involved waveform-related parameters, e.g., $a_{n,k}$, $b_{n,k}$ and $d_{n,k}$, are respectively given by,

$$a_{n,k} = \frac{8\pi^2 |\alpha_{n,k}|^2 f_s P \rho_n \bar{f}_n^2}{\sigma_z^2}, \quad (18a)$$

$$b_{n,k} = \frac{4\pi |\alpha_{n,k}|^2 f_s P \rho_n \mathfrak{T}\{\sigma_{tf}\}}{\sigma_z^2}, \quad (18b)$$

$$d_{n,k} \approx \frac{8\pi^2 |\alpha_{n,k}|^2 f_s P \rho_n \bar{t}_n^2}{\sigma_z^2}, \quad (18c)$$

where the approximation holds in (18c) when the effective time width meets $\tau_{n,k} \ll T_{\text{eff}}$. The relevant geometric spread parameters, including $\beta_{n,k}$, $\zeta_{n,k}$, $\xi_{n,k}$, $\varrho_{n,k}$, $\eta_{n,k}$ and $\kappa_{n,k}$, are omitted here and can be referred to [34], [42].

To visualize the relationship between the CRLBs and the PA coefficients, we now reformulate the CRLB expressions. Given the equivalent location FIM Let p_{ij} denote the $\{i, j\}$ th element of matrix \mathbf{P} , similar for v_{ij} and y_{ij} . The elements p_{ij} , v_{ij} and y_{ij} can be expressed as the weighted sum of ρ_n , i.e.,

$$\begin{cases} p_{ij} = \sum_{n=1}^N w_n^{p_{ij}} \rho_n = \boldsymbol{\rho}^T \mathbf{w}_{p_{ij}}, \\ v_{ij} = \sum_{n=1}^N w_n^{v_{ij}} \rho_n = \boldsymbol{\rho}^T \mathbf{w}_{v_{ij}}, \\ y_{ij} = \sum_{n=1}^N w_n^{y_{ij}} \rho_n = \boldsymbol{\rho}^T \mathbf{w}_{y_{ij}}, \end{cases} \quad (19)$$

where $w_n^{p_{ij}}$ is the n th element of the weight vector $\mathbf{w}_{p_{ij}}$, similar for $w_n^{v_{ij}}$ and $w_n^{y_{ij}}$. These weights can be readily obtained from (15)-(17) by extracting the PA vector $\boldsymbol{\rho}$.

By substituting (19) into (13), the CRLB matrix for location estimation can be rewritten as,

$$\mathbf{C}_L = \frac{1}{|\mathbf{U}|} \begin{bmatrix} u_{22} & -u_{12} \\ -u_{21} & u_{11} \end{bmatrix}, \quad (20)$$

where $|\mathbf{U}| = u_{11}u_{22} - u_{12}u_{21}$ and

$$u_{11} = \frac{1}{|\mathbf{Y}|} [\boldsymbol{\rho}^T (\mathbf{w}_{p_{11}} \boldsymbol{\rho}^T \mathbf{W}_y - \mathbf{w}_{v_{11}} \boldsymbol{\rho}^T \mathbf{W}_{12}^y - \mathbf{w}_{v_{12}} \boldsymbol{\rho}^T \check{\mathbf{W}}_{11}^y) \boldsymbol{\rho}], \quad (21a)$$

$$u_{12} = \frac{1}{|\mathbf{Y}|} [\boldsymbol{\rho}^T (\mathbf{w}_{p_{12}} \boldsymbol{\rho}^T \mathbf{W}_y - \mathbf{w}_{v_{21}} \boldsymbol{\rho}^T \mathbf{W}_{12}^y - \mathbf{w}_{v_{22}} \boldsymbol{\rho}^T \check{\mathbf{W}}_{11}^y) \boldsymbol{\rho}], \quad (21b)$$

$$u_{22} = \frac{1}{|\mathbf{Y}|} [\boldsymbol{\rho}^T (\mathbf{w}_{p_{22}} \boldsymbol{\rho}^T \mathbf{W}_y - \mathbf{w}_{v_{21}} \boldsymbol{\rho}^T \mathbf{W}_{22}^y - \mathbf{w}_{v_{22}} \boldsymbol{\rho}^T \check{\mathbf{W}}_{21}^y) \boldsymbol{\rho}], \quad (21c)$$

where $|\mathbf{Y}| = \boldsymbol{\rho}^T \mathbf{W}_y \boldsymbol{\rho}$. Elements u_{ij} are respectively given by,

$$\begin{cases} \mathbf{W}_y = \mathbf{w}_{y_{11}} \mathbf{w}_{y_{22}}^T - \mathbf{w}_{y_{12}} \mathbf{w}_{y_{21}}^T, \\ \mathbf{W}_{12}^y = \mathbf{w}_{v_{11}} \mathbf{w}_{y_{22}}^T - \mathbf{w}_{v_{12}} \mathbf{w}_{y_{21}}^T, \\ \mathbf{W}_{22}^y = \mathbf{w}_{v_{21}} \mathbf{w}_{y_{22}}^T - \mathbf{w}_{v_{22}} \mathbf{w}_{y_{21}}^T, \\ \check{\mathbf{W}}_{11}^y = \mathbf{w}_{v_{12}} \mathbf{w}_{y_{11}}^T - \mathbf{w}_{v_{11}} \mathbf{w}_{y_{12}}^T, \\ \check{\mathbf{W}}_{21}^y = \mathbf{w}_{v_{22}} \mathbf{w}_{y_{11}}^T - \mathbf{w}_{v_{21}} \mathbf{w}_{y_{12}}^T. \end{cases} \quad (22)$$

Similarly, the velocity CRLB matrix can be rewritten as,

$$\mathbf{C}_V = \frac{1}{|\mathbf{H}|} \begin{bmatrix} h_{22} & -h_{12} \\ -h_{21} & h_{11} \end{bmatrix}, \quad (23)$$

where $|\mathbf{H}| = h_{11}h_{22} - h_{12}h_{21}$. Elements h_{ij} are respectively given by,

$$h_{11} = \frac{1}{|\mathbf{P}|} [\boldsymbol{\rho}^T (\mathbf{w}_{y_{11}} \boldsymbol{\rho}^T \mathbf{W}_p - \mathbf{w}_{v_{11}} \boldsymbol{\rho}^T \mathbf{W}_{12}^p - \mathbf{w}_{v_{21}} \boldsymbol{\rho}^T \check{\mathbf{W}}_{11}^p) \boldsymbol{\rho}], \quad (24a)$$

$$h_{12} = \frac{1}{|\mathbf{P}|} [\boldsymbol{\rho}^T (\mathbf{w}_{y_{12}} \boldsymbol{\rho}^T \mathbf{W}_p - \mathbf{w}_{v_{12}} \boldsymbol{\rho}^T \mathbf{W}_{12}^p - \mathbf{w}_{v_{22}} \boldsymbol{\rho}^T \check{\mathbf{W}}_{11}^p) \boldsymbol{\rho}], \quad (24b)$$

$$h_{22} = \frac{1}{|\mathbf{P}|} [\boldsymbol{\rho}^T (\mathbf{w}_{y_{22}} \boldsymbol{\rho}^T \mathbf{W}_p - \mathbf{w}_{v_{12}} \boldsymbol{\rho}^T \mathbf{W}_{22}^p - \mathbf{w}_{v_{22}} \boldsymbol{\rho}^T \check{\mathbf{W}}_{21}^p) \boldsymbol{\rho}], \quad (24c)$$

where $|\mathbf{P}| = \boldsymbol{\rho}^T \mathbf{W}_p \boldsymbol{\rho}$, and

$$\begin{cases} \mathbf{W}_p = \mathbf{w}_{p_{11}} \mathbf{w}_{p_{22}}^T - \mathbf{w}_{p_{12}} \mathbf{w}_{p_{21}}^T, \\ \mathbf{W}_{12}^p = \mathbf{w}_{v_{11}} \mathbf{w}_{p_{22}}^T - \mathbf{w}_{v_{21}} \mathbf{w}_{p_{21}}^T, \\ \mathbf{W}_{22}^p = \mathbf{w}_{v_{12}} \mathbf{w}_{p_{22}}^T - \mathbf{w}_{v_{22}} \mathbf{w}_{p_{21}}^T, \\ \check{\mathbf{W}}_{11}^p = \mathbf{w}_{v_{21}} \mathbf{w}_{p_{11}}^T - \mathbf{w}_{v_{11}} \mathbf{w}_{p_{12}}^T, \\ \check{\mathbf{W}}_{21}^p = \mathbf{w}_{v_{22}} \mathbf{w}_{p_{11}}^T - \mathbf{w}_{v_{12}} \mathbf{w}_{p_{12}}^T. \end{cases} \quad (25)$$

IV. PROBLEM FORMULATION

In general, a higher power budget leads to improved sensing and communication performance. This section investigates a novel PA scheme aimed at maximizing the overall performance of CF MIMO-ISAC systems. Depending on specific application requirements, the optimization objective can be either sensing or communication performance, while the quality of service (QoS) requirement of the other function is incorporated as a constraint in the optimization model.

Let $\boldsymbol{\rho}_{\min} = [\rho_{\min,1}, \rho_{\min,2}, \dots, \rho_{\min,N}]^T$ denote the minimum PA coefficient to satisfy the so-called larger SNR for tight CRLBs, and $\boldsymbol{\rho}_{\max} = [\rho_{\max,1}, \rho_{\max,2}, \dots, \rho_{\max,N}]^T$ denote the maximum PA coefficient due to the power budgets of individual transmitters [13], [40]. In this paper, we consider

maximizing the communication data rate or SINR under the constraint of the sensing performance, i.e.,

$$\arg \min_{\boldsymbol{\rho}} -\boldsymbol{\rho}^T \mathbf{g}, \quad (26a)$$

$$\text{s.t. } \boldsymbol{\rho}^T \mathbf{1} = 1, \quad (26b)$$

$$\boldsymbol{\rho}_{\min} \leq \boldsymbol{\rho} \leq \boldsymbol{\rho}_{\max}, \quad (26c)$$

$$\text{tr}\{\mathbf{C}_L\} \leq \delta_l^2, \quad (26d)$$

$$\text{tr}\{\mathbf{C}_V\} \leq \delta_v^2, \quad (26e)$$

where δ_l^2 and δ_v^2 denote the corresponding performance thresholds³.

Similar to the approaches in [11], [13], [40], [49], we assume that the target's RCS, location, and velocity have been coarsely estimated by the ISAC system and are periodically updated over time⁴. Therefore, the PA coefficient vector $\boldsymbol{\rho}$ becomes the sole optimization variable, while the other relevant parameters are implicitly embedded through their coupling in equations (22) and (25).

V. ALGORITHM DERIVATION

In this section, we investigate the optimal PA strategy for maximizing the ISAC performance, as formulated in (57a)-(26e). However, the strong nonlinearity and non-convexity of the CRLB-based constraints in (26d) and (26e) render the problem analytically intractable. To overcome this challenge, we adopt a conjugate gradient (CG) iterative algorithm, enhanced with a penalty function and projection operator, to provide an efficient numerical solution.

We first introduce a penalty (function) for violating the nonlinear inequality constraints in (26c)-(26e)

$$\alpha(\boldsymbol{\rho}) = \tilde{f}_l(\boldsymbol{\rho}) + \tilde{f}_v(\boldsymbol{\rho}) + \sum_{n=1}^N (f_{\min,n}(\boldsymbol{\rho}) + f_{\max,n}(\boldsymbol{\rho})), \quad (27)$$

where

$$\begin{cases} \tilde{f}_l(\boldsymbol{\rho}) = (\max\{0, f_l(\boldsymbol{\rho})\})^q, \\ \tilde{f}_v(\boldsymbol{\rho}) = (\max\{0, f_v(\boldsymbol{\rho})\})^q, \\ f_{\min,n}(\boldsymbol{\rho}) = (\max\{0, \rho_{\min,n} - \rho_n\})^q, \\ f_{\max,n}(\boldsymbol{\rho}) = (\max\{0, \rho_n - \rho_{\max,n}\})^q, \end{cases} \quad (28)$$

with $f_l(\boldsymbol{\rho}) \triangleq \text{tr}\{\mathbf{C}_L\} - \delta_l^2$ and $f_v(\boldsymbol{\rho}) \triangleq \text{tr}\{\mathbf{C}_V\} - \delta_v^2$. We consider $q = 2$ to guarantee the continuous differentiable penalty functions. Then, the objective function for the penalty problem can be written as

$$L(\boldsymbol{\rho}) = -\boldsymbol{\rho}^T \mathbf{g} + \mu \alpha(\boldsymbol{\rho}). \quad (29)$$

As mentioned in [54], as the penalty factor μ is made large, the points generated for minimizing (29) approach an optimal solution of the original objective function (57a) from *outside the feasible region* and the iteration process terminate with $\mu \alpha(\boldsymbol{\rho}) \leq \epsilon_\mu$ for a small threshold $\epsilon_\mu > 0$. This issue can be

solved by setting ϵ_μ small enough or employing much tighter thresholds than the required bounds to some extent to mitigate the loss due to the non-zero threshold ϵ_μ .

On the other hand, intuitively, when orthogonal waveforms are employed, increasing the transmission power—or equivalently, the signal-to-noise ratio (SNR)—at any individual transmitter enhances both sensing and communication performance. Therefore, it is desirable to fully utilize the total power budget, as specified in (26b). To enforce this equality constraint and reduce both computational complexity and the nonlinearity of the optimization problem, we adopt a projection operator instead of incorporating another penalty sub-function

$$\boldsymbol{\rho}(\boldsymbol{\varpi}) = \boldsymbol{\Theta} \boldsymbol{\varpi} + \boldsymbol{\rho}_0, \quad (30)$$

where $\boldsymbol{\Theta} \triangleq \mathbf{I}_{N \times N} - \frac{\mathbf{1}_N \mathbf{1}_N^T}{N}$ is a projection matrix onto the zero space of $\mathbf{1}_N$. It is evident that $\mathbf{1}_N^T \boldsymbol{\rho}(\boldsymbol{\varpi}) = 1$ holds with $\mathbf{1}_N^T \boldsymbol{\rho}_0 = 1$. Thus, $\boldsymbol{\rho}(\boldsymbol{\varpi})$ is the sum of a constant PA vector $\boldsymbol{\rho}_0$ and a projection of any $N \times 1$ vector $\boldsymbol{\varpi}$ onto the zero space of $\mathbf{1}_N$. According to (30), the objective function can be further written as,

$$\mathcal{L}(\boldsymbol{\varpi}) = -\boldsymbol{\rho}^T(\boldsymbol{\varpi}) \mathbf{g} + \mu \alpha(\boldsymbol{\rho}(\boldsymbol{\varpi})). \quad (31)$$

This objective function makes all the constraints satisfied and thus convert the original constrained optimization regarding $\boldsymbol{\rho}$ into an unconstrained one regarding $\boldsymbol{\varpi}$.

A. Modified Conjugate Gradient Algorithm

We now propose a projection based modified CG (MCG) algorithm to minimize (31). Taking the derivative $\mathcal{L}(\boldsymbol{\varpi})$ regarding $\boldsymbol{\varpi}$ yields

$$\nabla \mathcal{L}(\boldsymbol{\varpi}) = \boldsymbol{\Theta} \nabla L(\boldsymbol{\rho}) = \boldsymbol{\Theta} [\mathbf{g} + \nabla \alpha(\boldsymbol{\rho})]. \quad (32)$$

where

$$\begin{aligned} \nabla \alpha(\boldsymbol{\rho}) &= \mu (\nabla \tilde{f}_l(\boldsymbol{\rho}) + \nabla \tilde{f}_v(\boldsymbol{\rho}) \\ &\quad + \sum_{n=1}^N (\nabla f_{\min,n}(\boldsymbol{\rho}) + \nabla f_{\max,n}(\boldsymbol{\rho}))), \end{aligned} \quad (33)$$

with components

$$\begin{cases} \nabla \tilde{f}_l(\boldsymbol{\rho}) = 2 \max\{f_l(\boldsymbol{\rho}), 0\} \nabla f_l(\boldsymbol{\rho}) \\ \nabla \tilde{f}_v(\boldsymbol{\rho}) = 2 \max\{f_v(\boldsymbol{\rho}), 0\} \nabla f_v(\boldsymbol{\rho}) \\ \nabla f_{\min,n}(\boldsymbol{\rho}) = 2 \min\{\rho_n - \rho_{\min,n}, 0\} \mathbf{e}_n \\ \nabla f_{\max,n}(\boldsymbol{\rho}) = 2 \max\{\rho_n - \rho_{\max,n}, 0\} \mathbf{e}_n. \end{cases} \quad (34)$$

Note that \mathbf{e}_n is an index vector with its element at index n being 1 and the others being zeros.

Solving (31) using an iterative method yields the update

$$\boldsymbol{\varpi}_{i+1} = \boldsymbol{\varpi}_i + v_i \mathbf{d}_i, \quad (35)$$

where \mathbf{d}_i is the descent direction of $\mathcal{L}(\boldsymbol{\varpi}_i)$ and v_i is the step size. The descent direction using the MCG is updated by

$$\mathbf{d}_{i+1} = -\boldsymbol{\Theta} \nabla L(\boldsymbol{\rho}_{i+1}) + \varsigma_i \mathbf{d}_i, \quad (36)$$

where ς_i denotes the deflection factor that characterizes a particular CG algorithm. Note that $-\boldsymbol{\Theta} \nabla L(\boldsymbol{\rho}_i)$ is still the descent direction of $L(\boldsymbol{\rho}_i)$ with $-\nabla L(\boldsymbol{\rho}_i)^T \boldsymbol{\Theta} \nabla L(\boldsymbol{\rho}_i) \leq 0$

³The thresholds can be set by referring to the CRLBs under a uniform power allocation.

⁴The previously estimated target parameters can be reused for PA optimization at the current time step, particularly in consecutive estimation or target tracking scenarios.

since the projection operator Θ is a symmetric positive definite matrix.

Given the initial direction $\mathbf{d}_1 = -\Theta \nabla L(\boldsymbol{\rho}_1)$, and using the idempotent property of the projection matrix, i.e., $\Theta^2 = \Theta$, we have $\Theta \mathbf{d}_i = \mathbf{d}_i$, $\forall i > 0$. Then, taking the projection of (35) leads to

$$\boldsymbol{\rho}_{i+1} = \boldsymbol{\rho}_i + v_i \mathbf{d}_i. \quad (37)$$

which has the same form as (35). Therefore, we hereafter directly adopt the update in (37). Moreover, note that the equality constraint $\mathbf{1}_N^T \boldsymbol{\rho}_i = 1$ holds for all $i > 1$ if and only if $\mathbf{1}_N^T \boldsymbol{\rho}_1 = 1$. This property follows from the iteration rules in (36) and (37).

To enable the convergence, it is necessary to develop a suitable step size v_i and search direction \mathbf{d}_i in each iteration to guarantee the non-increasing objective function i.e.,

$$L(\boldsymbol{\rho}_i + v_i \mathbf{d}_i) - L(\boldsymbol{\rho}_i) \leq 0. \quad (38)$$

Firstly, for the non-increasing search direction for each iteration i , it requires

$$\mathbf{d}_{i+1}^T \nabla L(\boldsymbol{\rho}_{i+1}) \leq 0, \quad (39)$$

where the equality holds if and only if $\nabla L(\boldsymbol{\rho}_{i+1}) = \mathbf{0}$. Using (36), we have,

$$\begin{cases} \varsigma_i \leq \varsigma_i^b, & \varsigma_i^b > 0 \\ \varsigma_i \geq \varsigma_i^b, & \varsigma_i^b < 0 \end{cases} \quad (40)$$

where ς_i^b is the bound for ς_i

$$\varsigma_i^b = \frac{\nabla L(\boldsymbol{\rho}_{i+1})^T \Theta \nabla L(\boldsymbol{\rho}_{i+1})}{\mathbf{d}_i^T \nabla L(\boldsymbol{\rho}_{i+1})}. \quad (41)$$

Note that $\nabla L(\boldsymbol{\rho}_{i+1})^T \Theta \nabla L(\boldsymbol{\rho}_{i+1}) > 0$ for any non-zero gradient $\nabla L(\boldsymbol{\rho}_{i+1})$ due to the positive definite Θ .

When considering inexact line searches, Hestenes and Stiefel's [55], [56] choice for ς_i can be preferable. We have the modified HS deflection,

$$\varsigma_i^{\text{HS}} = \frac{\nabla L(\boldsymbol{\rho}_{i+1})^T \mathbf{q}_i}{\mathbf{d}_i^T \mathbf{q}_i}, \quad (42)$$

which is obtained from $\mathbf{d}_{i+1}^T \mathbf{q}_i = 0$ with $\mathbf{q}_i \triangleq \Theta[\nabla L(\boldsymbol{\rho}_{i+1}) - \nabla L(\boldsymbol{\rho}_i)]$. In fact, when using the MCG algorithm, the orthogonality is desired between the (conjugate) gradients in adjacent iterations, i.e.,

$$|\mathbf{d}_i^T \nabla L(\boldsymbol{\rho}_{i+1})| \ll |\mathbf{d}_i^T \nabla L(\boldsymbol{\rho}_i)|, \quad (43)$$

$$|\nabla L(\boldsymbol{\rho}_{i+1})^T \Theta \nabla L(\boldsymbol{\rho}_i)| \ll |\nabla L(\boldsymbol{\rho}_{i+1})^T \Theta \nabla L(\boldsymbol{\rho}_{i+1})|. \quad (44)$$

Equations (43) and (44) ensure the positivity of both $\mathbf{d}_i^T \mathbf{q}_i$ and $\nabla L(\boldsymbol{\rho}_{i+1})^T \mathbf{q}_i$, respectively. This allow for a positive conjugate gradient scaling factor ς_i^{HS} . Furthermore, (43) and (44) also imply that $|\mathbf{d}_i^T \nabla L(\boldsymbol{\rho}_{i+1})| \ll |\mathbf{d}_i^T \mathbf{q}_i|$ and $|\nabla L(\boldsymbol{\rho}_{i+1})^T \mathbf{q}_i| \approx |\nabla L(\boldsymbol{\rho}_{i+1})^T \Theta \nabla L(\boldsymbol{\rho}_{i+1})|$, respectively. As a result, ς_i^{HS} is expected to be smaller than $|\varsigma_i^b|$, thereby satisfying the deflection constraint defined in (40).

Rather than strictly relying on the potentially tight and unquantifiable conjugacy conditions in (43) and (44), we instead enforce the positivity of both the numerator and denominator

in (42), along with the inequality $\varsigma_i^{\text{HS}} < |\varsigma_i^b|$. When these conditions hold, we set $\varsigma_i = \varsigma_i^{\text{HS}}$. Otherwise, we reset the MCG iteration by letting $\varsigma_i = 0$. To sum up, the deflection factor is updated by

$$\varsigma_i = \begin{cases} \varsigma_i^{\text{HS}}, & \min\{\nabla L(\boldsymbol{\rho}_{i+1})^T \mathbf{q}_i, \mathbf{d}_i^T \mathbf{q}_i, |\varsigma_i^b| - \varsigma_i^{\text{HS}}\} > 0, \\ 0, & \text{else.} \end{cases} \quad (45)$$

Note that, after every consecutive N MCG steps with $\varsigma_i = \varsigma_i^{\text{HS}}$, we will also let $\varsigma_i = 0$ to restart the new loop of MCG iteration. A proper reboot is potential in mitigating the accumulation of numerical errors, restoring the orthogonality and conjugacy of direction vectors, and avoiding local minima in nonlinear and non-convex optimization.

To optimize the step size selection, we define $f_i(v_i) \triangleq L(\boldsymbol{\rho}_i + v_i \mathbf{d}_i)$. Then, we have $f_i(0) = L(\boldsymbol{\rho}_i)$. The second-order Taylor approximation of $f_i(v_i)$ at $v_i = 0$ is given by

$$\begin{aligned} f_i(v_i) &\approx f_i(0) + v_i \nabla f_i(0) + v_i^2 \nabla^2 f_i(0)/2 \\ &= f_i(0) + v_i \mathbf{d}_i^T \nabla L(\boldsymbol{\rho}_i) + v_i^2 / 2 \mathbf{d}_i^T \nabla^2 L(\boldsymbol{\rho}_i) \mathbf{d}_i, \end{aligned} \quad (46)$$

where $\nabla^2 L(\boldsymbol{\rho}_i)$ is the Hessian matrix of $L(\boldsymbol{\rho})$ at $\boldsymbol{\rho}_i$. According to (39), we have $\mathbf{d}_i^T \nabla L(\boldsymbol{\rho}_i) \leq 0$. If $\|\nabla^2 L(\boldsymbol{\rho}_i)\|$ is locally bounded, there exists a non-negative step size bound v_b for given $\epsilon_L \in [0, 1)$ such that, when $v_i \leq v_b$, we have

$$f_i(v_i) - f_i(0) \leq \epsilon_L v_i \mathbf{d}_i^T \nabla L(\boldsymbol{\rho}_i). \quad (47)$$

When $\mathbf{d}_i^T \nabla^2 L(\boldsymbol{\rho}_i) \mathbf{d}_i \leq 0$, (47) always holds. In contrast, we have $v_b = \frac{2(\epsilon_L - 1) \mathbf{d}_i^T \nabla L(\boldsymbol{\rho}_i)}{\mathbf{d}_i^T \nabla^2 L(\boldsymbol{\rho}_i) \mathbf{d}_i}$ when $\mathbf{d}_i^T \nabla^2 L(\boldsymbol{\rho}_i) \mathbf{d}_i > 0$.

Due to the inherent high computational complexity of the Hessian matrix $\nabla^2 L(\boldsymbol{\rho}_i)$ in calculating v_b , we can apply an inexact line search (ILS) for the step size to enable

$$L(\boldsymbol{\rho}_i + v_i \mathbf{d}_i) - L(\boldsymbol{\rho}_i) \leq \epsilon_L v_i \mathbf{d}_i^T \nabla L(\boldsymbol{\rho}_i). \quad (48)$$

According to (39), the term on the right-hand side of (48) is always non-positive. Thus, (48) contributes to (38). The ILS controlling factor ϵ_L is used to control the decrement of the function $L(\boldsymbol{\rho})$ by moving a step v_i . When (48) is unmet for given v_i , it is scaled by,

$$v_i = \sigma_v v_i \quad (49)$$

where the scaling factor $\sigma_v \in (0, 1)$ and an initial step size is denoted as $v_i = v_{0,i}$.

On the other hand, the penalty function does not inherently guarantee that the individual power budget constraints at each transmitter are satisfied during the optimization process. As a result, negative PA values may emerge during intermediate iterations. These infeasible PA values can lead to misleading CRLB evaluations, such as yielding negative CRLBs instead of infinite ones, thereby artificially satisfying the CRLB constraints. To prevent unnecessary iterations within the infeasible region and to ensure physically meaningful results, it is essential to enforce non-negative PAs at each iteration step. To this end, the step size v_i needs to satisfy,

$$0 < v_i \leq v_i^b \quad (50)$$

Algorithm 1 The PP-MCG-ILS algorithm

Input: The positive scalar termination factor ϵ_μ and ϵ_{th} , small positive constant σ_v , ϵ_L and ϵ_v , initial penalty factor μ_1 , scaling factor $\varphi > 1$; initial PA parameter ρ_1 satisfying $\mathbf{1}^T \rho_1 = 1$, projection operator Θ , $\mathbf{y}_1 = \rho_1$, and $\mathbf{d}_1 = -\Theta \nabla L(\rho_1)$; a counter $k = 0$ and $i = j = 1$.

Output: The PA vector \mathbf{y}_j .

- 1: Step size: Calculate v_i^b according to (51); set $v_i = \epsilon_v v_i^b$, while $L(\rho_i + v_i \mathbf{d}_i) - L(\rho_i) > \epsilon_L v_i \mathbf{d}_i^T \nabla L(\rho_i)$, let $v_i = \sigma_v v_i$.
 - 2: Parameter update: $\rho_{i+1} = \rho_i + v_i \mathbf{d}_i$.
 - 3: Convergence condition: If $|L(\rho_{i+1}) - L(\rho_i)|/|L(\rho_{i+1})| \leq \epsilon_{th}$, $\mathbf{y}_j = \rho_{i+1}$, and go to step 5; Otherwise, go to next step.
 - 4: Direction update: According to (45), if $\varsigma_i = \varsigma_i^{HS}$, $k = k + 1$, or $k = 0$ otherwise; when $k = N$, let $\varsigma_i = 0$ and $k = 0$; update $\mathbf{d}_{i+1} = -\Theta \nabla L(\rho_{i+1}) + \varsigma_i \mathbf{d}_i$; let $i = i + 1$, and go back to step 1.
 - 5: Penalty update: If $\mu_j \alpha(\mathbf{y}_j) < \epsilon_\mu$, stop; Otherwise, let $\mu_{j+1} = \varphi \mu_j$, and $\mathbf{d}_{i+1} = -\Theta \nabla L(\rho_{i+1})$; let $j = j + 1$ and $i = i + 1$, and go to step 1.
-

where v_i^b is a step size upper bound given by

$$v_i^b = \min_{d_{n,i} < 0} \{\rho_{n,i}/|d_{n,i}|\}, \quad (51)$$

with $\rho_{n,i}$ denoting the n th element of ρ_i and similar for $d_{n,i}$. Thus, the initial step size for ILS can be selected as,

$$v_{0,i} = \epsilon_v v_i^b \quad (52)$$

with $\epsilon_v \in (0, 1]$. Note that there must exist $d_{n,i} < 0$ at each iteration i unless $\mathbf{d}_i = \mathbf{0}$ due to $\sum_{n=1}^N d_{n,i} = 0$. The ILS method characterized in (48)-(52) can be seen as the extension and application of the Armijo's Rule [56], [57] in our work.

A termination condition is significant for the iterative algorithm. A natural choice, based on the ILS condition in (48), is that the absolute difference in objective function values between consecutive iterations satisfies $|L(\rho_{i+1}) - L(\rho_i)| \leq \epsilon$ where ϵ is a small positive threshold. To avoid numerical instability arising from the magnitude of the objective function itself, we apply a normalized termination condition, i.e., $|L(\rho_{i+1}) - L(\rho_i)|/|L(\rho_{i+1})| \leq \epsilon_{th}$, as employed in both the MCG-based and MSD-based algorithms.

We now present the Penalty-function and Projection-based Modified Conjugate Gradient algorithm with inexact line search (PP-MCG-ILS). A large penalty factor may lead to computational issues, such as an ill-conditioned Hessian matrix, which can adversely affect the convergence of the MCG algorithm. To mitigate this, we adopt a strategy of progressively increasing the penalty factor across iterations. For given penalty factor μ_k , the MCG algorithm is executed until its termination condition is satisfied. Then, the penalty factor is updated as $\mu_{k+1} = \varphi \mu_k$ for the next loop of penalty-based iteration, where $\varphi > 1$ is a scaling constant. This process continues until the convergence criterion $\mu_k \alpha(\rho) \leq \epsilon_\mu$ is met, with ϵ_μ being a small, user-defined threshold [54]. This approach ensures numerical stability and gradual enforcement of the constraint. The complete PP-MCG-ILS algorithm is summarized in Algorithm 1.

B. Modified steepest descent algorithm

In fact, alternative unconstrained optimization methods can also be employed to solve the proposed projection-based penalty problem in (31). For comparison purposes, we also develop a Modified Steepest Descent (MSD) algorithm, adapted

from the proposed MCG framework. The primary distinction between the MSD and MCG algorithms lies in the choice of the descent direction. Specifically, in the MSD method, the descent direction at each iteration is directly set as the negative gradient of the objective function

$$\mathbf{d}_i = -\Theta \nabla L(\rho_i), \quad (53)$$

which can be directly obtained from MCG by setting the deflection factor to zero. We herein omit the detailed implementation steps of PP-MSD-ILS since they can be obtained from the PP-MCG-ILS by simply revising step 4 of Algorithm 1.

C. Benchmarks

We now introduce two benchmark algorithms, derived from the PP-MCG-ILS and PP-MSD-ILS frameworks, respectively. These benchmark variants adopt fixed step sizes at each iteration instead of employing ILS. To mitigate potential instability arising from overly large or small gradient magnitudes under fixed step updates, we normalize the update directions using their l_2 -norm. For the Penalty-function and Projection driven Normalized Steepest Descent (PP-NSD) algorithm, the descent direction is defined as

$$\mathbf{d}_i = -\mathbf{g}_i / (\|\mathbf{g}_i\|_2 + \epsilon_d), \quad (54)$$

where $\mathbf{g}_i = \Theta \nabla L(\rho_i)$, and ϵ_d is a small constant to prevent division by zero. Similarly, for the penalty function and projection driven normalized CG (PP-NCG) algorithm, the descent direction is given by,

$$\mathbf{d}_{i+1} = -(\mathbf{g}_{i+1} + \varsigma_i \mathbf{d}_i) / (\|\mathbf{g}_{i+1} + \varsigma_i \mathbf{d}_i\|_2 + \epsilon_d), \quad (55)$$

where the deflection factor ς_i is computed by (45).

The step size selection in both benchmark algorithms is

$$v_i = \min\{\epsilon_v v_i^b, v_0\}, \quad (56)$$

with v_i^b provided by (51) and v_0 being a predetermined step size. Additionally, the descent function (38) may not hold when utilizing the fixed step sizes. Therefore, it is necessary to provide a sufficiently large integer I as the upper bound of the number of iterations. In the same vain, due to the non-monotonic penalty function, the minimum may not occur at the final iteration but within a few steps before it. To address this, we introduce an alternative penalty stopping criterion given by $\mu_j \min_{i+1-S \leq q \leq i+1} \{\alpha(\rho_q)\} < \epsilon_\mu$ where S represents the window size for searching the minimum penalty value over recent iterations. The detailed implementation steps of the PP-NSD algorithm are omitted here, as it can be readily constructed by modifying step 4 of the PP-NCG algorithm described in Algorithm 2.

VI. EXTENSION TO PURE SENSING

In this section, we propose a Penalty-function based Normalized Conjugate Gradient algorithm with inexact line search (P-NCG-ILS) for the PA in pure sensing scenario. We consider

Algorithm 2 The PP-NCG algorithm

Input: Positive scalar termination factor ϵ_μ and ϵ_{th} , a large integer I and a small integer S , small positive constants σ_v , ϵ_L , ϵ_d and ϵ_v , initial step size v_0 , initial penalty factor μ_1 and its scaling factor $\varphi > 1$; initial PA parameter ρ_1 satisfying $\mathbf{1}^T \rho_1 = 1$, projection operator Θ , $\mathbf{y}_1 = \rho_1$, and $\mathbf{d}_1 = -\Theta \nabla L(\rho_1) / (\|\Theta \nabla L(\rho_1)\|_2 + \epsilon_d)$; a counter $k = 0$ and $i = j = 1$.
Output: The PA vector \mathbf{y}_j .

- 1: Step size: $v_i = \min\{\epsilon_v v_i^b, v_0\}$.
 - 2: Parameter update: $\rho_{i+1} = \rho_i + v_i \mathbf{d}_i$.
 - 3: Convergence condition: If $|L(\rho_{i+1}) - L(\rho_i)| / |L(\rho_{i+1})| \leq \epsilon_{th}$ or $i + 1 = I$, $\mathbf{y}_j = \rho_{i+1}$, go to step 5; Otherwise, go to next step.
 - 4: Direction update: According to (45), if $\varsigma_i = \varsigma_i^{HS}$, $k = k + 1$, or $k = 0$ otherwise; when $k = N$, let $\varsigma_i = 0$ and $k = 0$; update \mathbf{d}_{i+1} through (55); let $i = i + 1$, and go back to step 1.
 - 5: Penalty update: If $\mu_j \min_{i+1-S \leq q \leq i+1} \{\alpha(\rho_q)\} < \epsilon_\mu$, stop; Otherwise, let $\mu_{j+1} = \varphi \mu_j$, and $\mathbf{d}_{i+1} = -\Theta \nabla L(\rho_{i+1}) / (\|\Theta \nabla L(\rho_{i+1})\|_2 + \epsilon_d)$; let $j = j + 1$ and $i = i + 1$, and go to step 1.
-

Algorithm 3 The P-NCG-ILS algorithm

Input: Positive scalar termination factors ϵ_μ and ϵ_{th} , small positive constants σ_v , ϵ_L and ϵ_v , initial step size v_0 , initial penalty factor μ_1 and its scaling factor $\varphi > 1$; initial PA parameter ρ_1 satisfying $\mathbf{1}^T \rho_1 = 1$, $\mathbf{y}_1 = \rho_1$, and $\mathbf{d}_1 = -\nabla L_s(\rho_1) / \|\nabla L_s(\rho_1)\|_2$; a counter $k = 0$ and $i = j = 1$.
Output: The PA vector \mathbf{y}_j .

- 1: Step size: $v_i = \min\{\epsilon_v v_i^b, v_0\}$; while $L_s(\rho_i + v_i \mathbf{d}_i) - L_s(\rho_i) > \epsilon_L v_i \mathbf{d}_i^T \nabla L(\rho_i)$, let $v_i = \sigma_v v_i$.
 - 2: Parameter update: $\rho_{i+1} = \rho_i + v_i \mathbf{d}_i$.
 - 3: Convergence condition: If $|L_s(\rho_{i+1}) - L_s(\rho_i)| / |L_s(\rho_{i+1})| \leq \epsilon_{th}$, $\mathbf{y}_j = \rho_{i+1}$, and go to step 5; Otherwise, go to next step.
 - 4: Direction update: According to (45), if $\varsigma_i = \varsigma_i^{HS}$, $k = k + 1$, or $k = 0$ otherwise; when $k = N$, let $\varsigma_i = 0$ and $k = 0$; update $\mathbf{d}_{i+1} = \tilde{\mathbf{d}}_{i+1} / (\|\tilde{\mathbf{d}}_{i+1}\|_2 + \epsilon_d)$ with $\tilde{\mathbf{d}}_{i+1} = -\nabla L_s(\rho_{i+1}) + \varsigma_i \mathbf{d}_i$; let $i = i + 1$, and go back to step 1.
 - 5: Penalty update: If $\mu_j \alpha(\mathbf{y}_j) < \epsilon_\mu$, stop; Otherwise, let $\mu_{j+1} = \varphi \mu_j$, and $\mathbf{d}_{i+1} = -\nabla L_s(\rho_{i+1})$; let $j = j + 1$ and $i = i + 1$, and go to step 1.
-

the power minimization under power budget constraints and CRLB constraints, i.e.,

$$\arg \min_{\rho} \rho^T \mathbf{1}, \quad (57a)$$

$$\text{s.t. } \rho^T \mathbf{1} \leq 1, \quad (57b)$$

$$(26c), (26d) \text{ and } (26e). \quad (57c)$$

We present the penalty function as follows

$$\begin{aligned} \alpha_s(\rho) &= f_s(\rho) + \tilde{f}_l(\rho) + \tilde{f}_v(\rho) \\ &+ \sum_{n=1}^N (f_{\min,n}(\rho) + f_{\max,n}(\rho)), \end{aligned} \quad (58)$$

with the penalty function for the total power budget

$$f_s(\rho) = (\max\{0, \rho^T \mathbf{1} - 1\})^q. \quad (59)$$

Then, the objective function can be formulated as

$$L_s(\rho) = \rho^T \mathbf{1} + \mu \alpha_s(\rho). \quad (60)$$

The complete P-NCG-ILS algorithm is summarized in Algorithm 3.

VII. ALGORITHM ANALYSIS

The proposed algorithms (e.g., PP-MCG-ILS, PP-MSD-ILS and P-NCG-ILS) can be extended and applied to a broad class of nonlinear and non-convex optimization problems. These

problems are typically characterized by an affine equality constraint, if present, satisfied through a projection operator, along with nonlinear or non-convex constraints incorporated via penalty functions. The ILS mechanism is used to enhance convergence. In the following, we analyze the convergence behavior and computational complexity of the proposed algorithms.

A. Convergence analysis

We now provide the convergence condition of the proposed PP-MCG-ILS and PP-MSD-ILS algorithms. Before delving to the details, we define the increment of the parameter update and the objective function respectively as

$$\Delta \rho_{i+1} \triangleq \rho_{i+1} - \rho_i = v_i \mathbf{d}_i \quad (61)$$

and

$$\Delta L(\rho_{i+1}) \triangleq L(\rho_{i+1}) - L(\rho_i). \quad (62)$$

Lemma 1. *The sufficient and necessary condition for $\|\Delta \rho_{i+1}\| \rightarrow 0$ and $\Delta L(\rho_{i+1}) \rightarrow 0$ is that, there exists an integer I such that, $\mathbf{d}_i \rightarrow \mathbf{0}$ or $v_i \rightarrow 0$ when $i > I$.*

Proof. The proof is given in Appendix A. ■

Definition. A function $L(\rho)$ is Lipschitz gradient continuous over a set Ω , if there exists a constant $C > 0$, $\|\nabla L(\rho_i) - \nabla L(\rho_j)\| \leq C \|\rho_i - \rho_j\|$ for any $\rho_i, \rho_j \in \Omega$ [58], [59].

Theorem 1. *Given a nonempty convex set Ω where the objective function $L(\rho_i)$ is bounded over its interior points, if the objective function is Lipschitz gradient continuous over Ω , the ILS-based descent direction iterative algorithm will converge to a stationary point with a zero descent direction $\mathbf{d}_i \rightarrow \mathbf{0}$. In contrast, if it is not Lipschitz gradient continuous, the sequence $\{\rho_i\}$ and $\{L(\rho_i)\}$ may converge to a Lipschitz gradient noncontinuous point where the norm of the Hessian matrix may approach infinity.*

Proof. The proof is given in Appendix B. ■

Theorem 1 provides the convergence analysis for the proposed PP-MCG-ILS and PP-MSD-ILS algorithms.

We now prove the Lipschitz gradient continuity of the objectivity functions in (31) and (60).

The feasible domain $\Omega \subset \mathbb{R}^N$ is closed, bounded, and convex. All CRLB-involved matrices, e.g., $\mathbf{P}(\rho)$, $\mathbf{Y}(\rho)$, and their inverses are uniformly bounded and positive definite over the set Ω .

Firstly, each term $f_{\min,n}(\rho)$ and $f_{\max,n}(\rho)$ is piecewise quadratic, and its gradient is Lipschitz continuous due to continuity and boundedness. So does $f_s(\rho)$. Then, since $\mathbf{C}_L(\rho)$ is uniformly positive definite and smooth in ρ , it follows that: $f_l(\rho)$ is continuously differentiable, and so is

$$\nabla \tilde{f}_l(\rho) = \begin{cases} 2f_l(\rho) \nabla f_l(\rho), & \text{if } f_l(\rho) > 0 \\ 0, & \text{otherwise.} \end{cases} \quad (63)$$

Given that $\nabla f_l(\rho)$ is smooth and bounded (due to the matrix inverse being smooth on positive definite matrices), $\nabla \tilde{f}_l(\rho)$ is Lipschitz continuous. A similar argument applies to $\tilde{f}_v(\rho)$. Hence, $\nabla_{\rho} \alpha(\rho)$ and $\nabla_{\rho} \alpha_s(\rho)$ are Lipschitz continuous over Ω , and so are $\nabla_{\rho} L(\rho)$ and $\nabla_{\rho} L_s(\rho)$.

Additionally, since Θ is a constant matrix with $\|\Theta\|_2 = 1$, and $\nabla_{\rho} f(\rho)$ is Lipschitz continuous, the composition $\nabla \mathcal{L}(\varpi) = \Theta \nabla L(\rho)$ is also Lipschitz continuous. There exists a constant $C > 0$ such that $\forall \varpi_1, \varpi_2 \in \Omega_{\varpi}$

$$\|\nabla_{\varpi} \mathcal{L}(\varpi_1) - \nabla_{\varpi} \mathcal{L}(\varpi_2)\|_2 \leq C \|\varpi_1 - \varpi_2\|_2.$$

Therefore, $\mathcal{L}(\varpi)$ is Lipschitz gradient continuous on Ω_{ϖ} . ■

B. Complexity analysis

We observe that the additional computational complexity of the PP-MCG-ILS algorithm, compared to the PP-MSD-ILS algorithm, primarily stems from the computation of ζ_i^b and ζ_i^{HS} at each iteration, which requires approximately $4N$ multiplications and 2 divisions. In both algorithms, the dominant computational burden lies in evaluating the objective function during the ILS and computing the gradients for direction updates, which are inherently tied to the CRLB expressions. Therefore, a more meaningful comparison of total computational cost focuses on the number of ILS steps per iteration. This number is influenced by the step size threshold, given by the right-hand side of (67), the initial step size $v_{0,i}$ in (52), and the scaling factor. At a given iterate ρ_i , a larger descent direction norm $\|d_i\|$ generally leads to a smaller $v_{0,i}$ and a reduced step size threshold. As a result, the number of ILS steps is expected to be comparable between the PP-MCG-ILS and PP-MSD-ILS algorithms. Given this, the primary metrics for evaluating the relative performance of these two algorithms become their convergence rate and the quality of their steady-state solutions.

We now qualitatively compare the computational complexity between algorithms employing ILS and those without ILS. As previously discussed, the number of ILS steps significantly impacts the number of evaluations of the objective function. Thus, the computational complexity of the benchmark algorithms (without ILS) can be considerably lower at each iteration during step 1 compared to the PP-MCG-ILS and PP-MSD-ILS algorithms. However, all four algorithms have similar complexity in step 4 due to the inherently intensive gradient calculations involved. Moreover, the overall computational complexity heavily depends on the convergence rates, or equivalently, the total number of iterations required for convergence. As will be demonstrated in the subsequent simulation results, the proposed PP-MCG-ILS algorithm exhibits a notably higher convergence rate compared to its counterparts, with or without ILS. This superior convergence performance significantly reduces the overall computational effort, particularly benefiting the demanding computations of gradients.

VIII. SIMULATION RESULTS

In this section, we conduct some simulations to evaluate the proposed PP-MCG-ILS and PP-MSD-ILS algorithms for PA optimization. All APs, including N single antenna transmitters and K single antenna receivers, are assumed to be stationary. We employ the orthogonal chirp division multiplexing (OCDM) [60] waveform with a single Gaussian pulse shaping.

The carrier frequency is 3GHz. The lowpass equivalent is formulated by,

$$s_n(t) = (2/T^2)^{1/4} e^{-\pi t^2/T^2} e^{j\pi M/T^2(t-(n-1)T/M)^2}, \quad (64)$$

where M is the number of OCDM chirps, and T is proportional to the effective pulse time width.

A. CRLBs

We first verify the CRLB in comparison with the MLE results. To maintain consistency with existing works [34]–[36], [38]–[41], we use the signal energy-to-noise ratio (SENR), defined as $\tilde{\delta}_{\text{cn}} \triangleq P/\sigma_{\text{cn}}^2$, instead of the SCNR δ_{cn} in evaluating the CRLBs. Due to the high complexity of four-dimensional MLE, we consider a simple 4×3 nonsymmetric multi-static radar configuration given in Fig. 2(a). Consider the OCDM waveform with $M = 16$, $T = 10^{-2}$ s and a sampling rate of $f_s = 1$ kHz. The velocity of the target is $(20, 30)$ m/s.

Fig. 3 compares the mean squared error (MSE) of the MLE with the derived CRLB. It is observed that the derived CRLBs closely match the MSEs for SENR values above -20 dB. The small discrepancies in the low-SENR regime are attributed to the suboptimal behavior of the likelihood function under noise-dominated conditions. Overall, these results validate the effectiveness and accuracy of the proposed CRLBs.

B. Power Allocation for ISAC

The performance of the proposed PA algorithms is evaluated by comparison with the PP-NCG and PP-NSD benchmark algorithms. To ensure communication quality, a larger number of APs are designated for transmitting ISAC signals, while a smaller subset is used for receiving target-reflected signals. Without loss of generality, we consider a CF MIMO-ISAC system comprising 10 transmitters and 2 receivers, as illustrated in Fig. 2(b). To guarantee the CRLB effectiveness, we assume the minimum PA coefficient vector is $\rho_{\min} = 0.01 \times \mathbf{1}_N$. The PA budget is $\rho_{\max} = 0.3 \times \mathbf{1}_N$. Consider a target moving slowly with velocity $l_v = [4, 5] \text{ m/s}$. A typical modulus squared RCS matrix is given by $\begin{bmatrix} 0.37 & 0.70 & 1.38 & 0.65 & 2.40 & 0.18 & 0.25 & 0.82 & 0.14 & 0.35 \\ 0.40 & 2.05 & 1.14 & 0.42 & 0.03 & 0.11 & 2.02 & 1.65 & 1.24 & 3.65 \end{bmatrix}^T$. The channel gains between the user and the transmitters are assumed to be $[2.11, 12.57, 5.63, 0.75, 0.61, 1.75, 0.20, 2.34, 14.79, 9.68]^T$. In this ISAC setup, the CRLB thresholds for the position and velocity are given by $[250, 0.13]$.

The PA vector is initialized as the normalized PA vector $\rho_1 = \mathbf{1}_N/N$, unless noted otherwise. The initial penalty factor is set to be $\mu_1 = 10^4$. We hereafter consider the ILS controlling factor $\epsilon_L = 1e-3$, the initial step size controlling factor $\epsilon_v = 0.9$, the penalty factor scaling coefficient $\phi = 10$, and the penalty threshold $\epsilon_{\mu} = 10^{-3}$, unless noted otherwise. The other simulation conditions are given in Table I. Note that the presented SINRs, PA vectors, and CRLBs, are obtained by averaging 100 points after convergence.

Firstly, we evaluate the convergence and steady-state performance of the proposed algorithms. The SINR learning curves of four algorithms are illustrated in Fig. 4. As apparently

TABLE I: Simulation parameters

Algorithms	PP-MCG-ILS	PP-MSD-ILS	PP-NCG	PP-NSD
Fig. 4	$\{\epsilon_{th}, \sigma_v\} = \{1e-11, 0.5\}$	same as PP-MCG-ILS	$v \in \{4e-5, 2e-5\}$	same as PP-NCG
Figs. 5 and 6	same as Fig. 4	—	$v = 2e-5$	—
Figs. 7 and 8	$\epsilon_{th} = 1e-12, \sigma_v = 0.7$	same as PP-MCG-ILS	$v = 2e-5$	same as PP-NCG
Figs. 9 and 10	$\{\epsilon_{th}, \sigma_v\} = \{1e-11, 0.7\}$	—	—	—

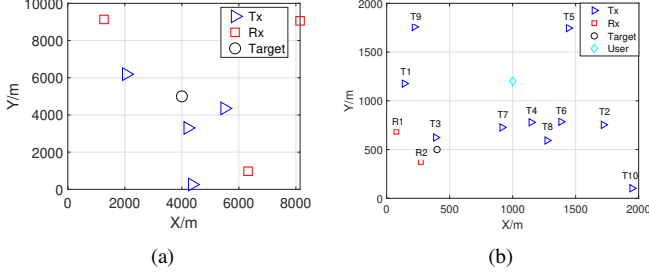
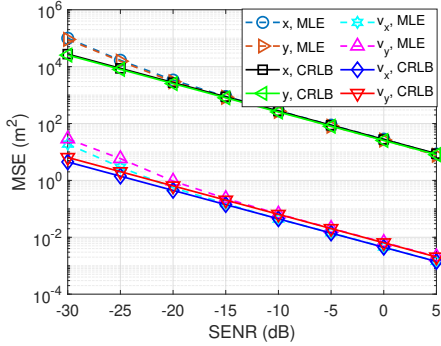
Fig. 2: The AP location distribution of the ISAC system: (a) 4×3 radar setting; (b) CF MIMO-ISAC setting.

Fig. 3: The MSE versus the SENRLB under different SENRs.

seen in Fig. 4, the PP-MCG-ILS has the highest convergence rate, followed by the PP-MSD-ILS, while the counterparts without ILS presents comparatively slow convergence. Additionally, the benchmark algorithms without ILS exhibit numerical fluctuations, particularly under large fixed step sizes. This behavior suggests potential instability and divergence risks. Consequently, we refrain from increasing the step sizes further during simulations to avoid compromising convergence reliability.

The evolution of the PA coefficients and corresponding CRLB values with respect to the number of iterations is illustrated in Fig. 5 and Fig. 6, respectively. The results show that the PP-MCG-ILS algorithm achieves significantly faster convergence compared to the PP-NCG algorithm. Ultimately, all four algorithms converge to a common PA vector, given by $\rho = [0.01, 0.30, 0.0638, 0.01, \dots, 0.01, 0.30, 0.2762]^T$, which satisfies the sensing QoS constraints. Notably, more power is allocated to transmitters 2, 9, and 11 due to their higher communication channel gains. Furthermore, the steady-state CRLB values remain within the predefined threshold limits, confirming the validity and effectiveness of the proposed optimization framework.

The proposed sequential penalty-based algorithms leverage the optimal solution from the previous iteration loop as the initial point for the current loop under an updated penalty

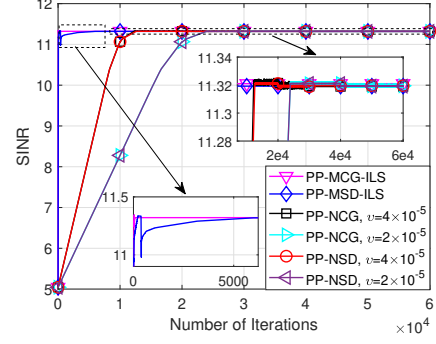
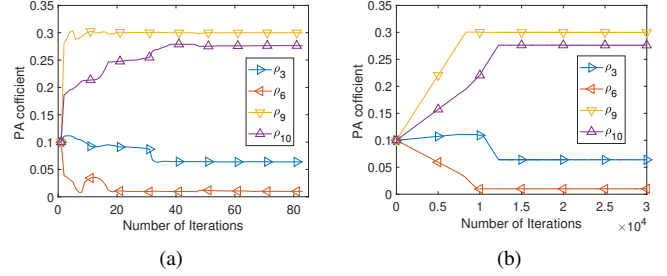
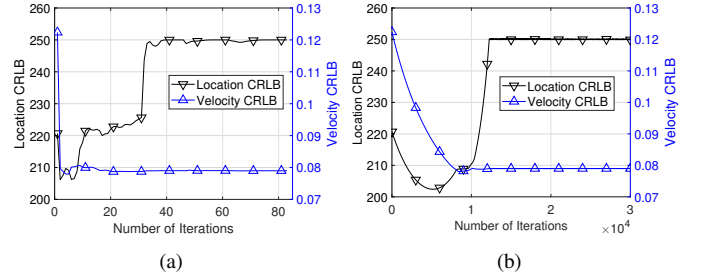


Fig. 4: SINR with sequential penalty factor

Fig. 5: PA coefficient: (a) PP-MCG-ILS; (b) PP-NCG with $v = 2 \times 10^{-5}$.Fig. 6: CRLB values: (a) PP-MCG-ILS; (b) PP-NCG with $v = 2 \times 10^{-5}$.

factor. To further explore the impact of initialization, we compare the performance of different initial PA strategies under a fixed penalty factor. In addition to the commonly used uniform PA initialization, we introduce a heuristic PA scheme, where the initial allocation is proportional to the communication channel gain, given by $\rho_1 = g / \sum_n |g_n|^2$. The results are illustrated in Figs. 7 and 8. When comparing to sequential penalty-based counterparts in Fig. 4, the PP-MCG-ILS and PP-NCG algorithms initialized with uniform PA exhibit similar convergence behavior. However, the PP-MSD-ILS and PP-NSD algorithms show degraded convergence, highlighting the superior convergence properties of CG-based

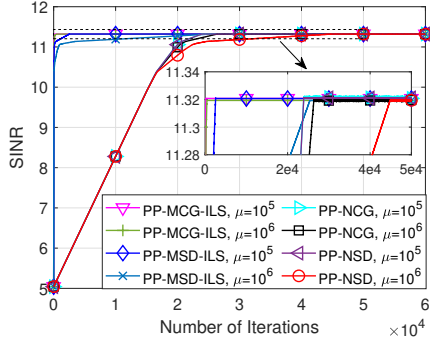


Fig. 7: SINR with initial uniform PA

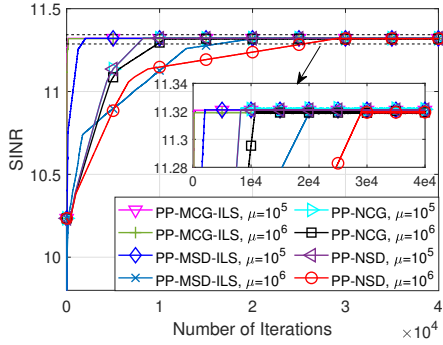


Fig. 8: SINR with initial heuristic PA

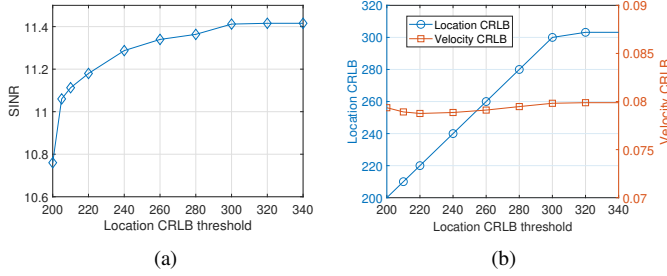


Fig. 9: Steady-state SINRs and CRLBs versus the location CRLB thresholds: (a) SINR; (b) CRLB.

algorithms over SD-based methods under identical conditions. When employing the heuristic PA initialization, all algorithms demonstrate significantly improved convergence rates compared to the uniform PA case. Moreover, both PP-NCG and PP-NSD achieve noticeable performance gains relative to their sequential penalty-based counterparts, particularly PP-NCG. In contrast, the PP-MCG-ILS algorithm shows robust and superior convergence behavior, and PP-MSD-ILS exhibits a slight degradation.

To summarize, the proposed algorithms exhibit superior convergence behavior under the sequential penalty framework, consistently outperforming the benchmark methods. While the benchmark algorithms can benefit from specific conditions, such as an empirically tuned penalty factor and a well-initialized starting point, their performance is less robust and generalizable. In contrast, the PP-MCG-ILS algorithm demonstrates consistently strong convergence and steady-state accuracy across a wide range of settings, irrespective of

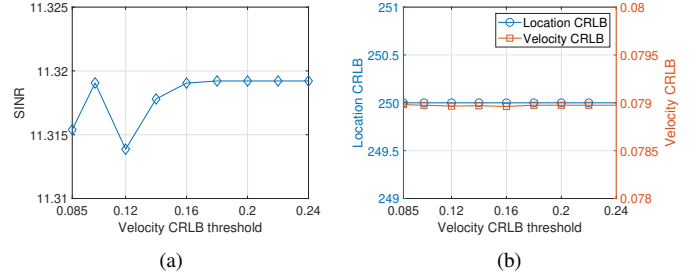


Fig. 10: Steady-state SINRs and CRLBs versus the velocity CRLB thresholds: (a) SINR; (b) CRLB.

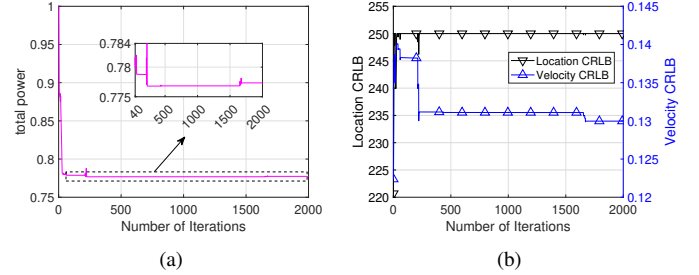


Fig. 11: Learning results for pure sensing: (a) total power; (b) CRLBs.

initialization or penalty factor selection.

We now investigate the impact of the CRLB thresholds on the performance of the proposed PP-MCG-ILS algorithm. As shown in Fig. 9(a), relaxing the location CRLB thresholds leads to a gradual increase in the steady-state SINR, which eventually stabilizes. This trend aligns with the behavior observed in Fig. 9(b), where the achieved location CRLB value closely approaches its threshold and then converge. Furthermore, it is noteworthy that the velocity CRLB remains largely unaffected by variations in the location CRLB thresholds. In contrast, Fig. 10 shows that the performance of the PP-MCG-ILS algorithm exhibits negligible variation with the increased velocity CRLB threshold. The observed CRLB saturation with respect to the corresponding CRLB threshold may be an inherent outcome of the introduced power budget constraints.

C. Power Allocation for pure sensing

We now simply verify the effectiveness of the proposed P-MCG-ILS algorithm for total power minimization in joint location and velocity estimation. The initial penalty factor is set to be $\mu_1 = 1$, $\sigma_v = 0.2$ and the penalty threshold $\epsilon_\mu = 10^{-6}$. The other simulation conditions are the same as the PP-MCG-ILS algorithm in Fig. 4.

The learning results for total power optimization and the corresponding CRLB performance are illustrated in Fig. 11. As seen in Fig. 11(a), the algorithm demonstrates rapid convergence. Under the same CRLB threshold settings, the total power consumption in the pure sensing scenario is significantly lower than that in the ISAC case. This is expected, as ISAC systems must allocate sufficient power to meet both sensing and communication requirements, particularly for maximizing communication performance. Moreover, both

the location and velocity CRLBs in the pure sensing case closely align with their respective thresholds. In contrast, in the ISAC scenario (refer to Fig. 6(a)), the velocity CRLB matches its threshold loosely. This difference arises because, in pure sensing, any enhancement in CRLB performance directly benefits from increased sensing power. However, in ISAC, power allocation is optimized primarily for communication performance, with CRLB constraints being satisfied, potentially loosely, within acceptable margins.

IX. CONCLUSIONS

This paper presents, for the first time, a comprehensive investigation of the power allocation problem in a cell-free (CF) MIMO-ISAC framework, where joint location and velocity estimation is considered as the sensing task. We employ newly derived approximate Cramér-Rao lower bounds (CRLBs) as sensing performance metrics, alongside user receive SINR as the communication metric. To address the inherent nonlinearity and non-convexity of the resulting optimization problem, we propose a penalty function and projection-based modified conjugate gradient algorithm with inexact line search (PP-MCG-ILS). Additionally, we introduce a penalty function-based normalized conjugate gradient algorithm with inexact line search (P-NCG-ILS) to handle the power minimization problem in pure sensing scenarios. We analyze the convergence behavior and qualitatively compare the computational complexity of all proposed methods. Simulation results confirm the accuracy of the derived CRLBs and demonstrate the efficacy of the proposed power allocation strategies in enhancing pure sensing and overall ISAC performance. The findings offer valuable insights into resource-efficient design for next-generation CF MIMO-ISAC networks and lay the groundwork for future extensions involving more complex sensing tasks and dynamic resource management.

APPENDIX A PROOF OF LEMMA 1

It is obvious that $\|\Delta\boldsymbol{\rho}_{i+1}\| \rightarrow 0$ when $i > I$ if and only if either $\mathbf{d}_i \rightarrow \mathbf{0}$ or $v_i \rightarrow 0$ when $i > I$. On the other hand, in light of (46), we have

$$\Delta L(\boldsymbol{\rho}_{i+1}) \approx v_i \mathbf{d}_i^T \nabla L(\boldsymbol{\rho}_i) + v_i^2 / 2 \mathbf{d}_i^T \nabla^2 L(\boldsymbol{\rho}_i) \mathbf{d}_i. \quad (65)$$

Firstly, if $\mathbf{d}_i \rightarrow \mathbf{0}$ or $v_i \rightarrow 0$ for $i > I$, we readily have $\Delta L(\boldsymbol{\rho}_{i+1}) \rightarrow 0$. Assume there exists $i > I$, where $\Delta L(\boldsymbol{\rho}_{i+1}) \rightarrow 0$ with neither $\mathbf{d}_i \rightarrow \mathbf{0}$ nor $v_i \rightarrow 0$. We can solve the step size for $\Delta L(\boldsymbol{\rho}_{i+1}) = 0$ as

$$v_i = \frac{-2\mathbf{d}_i^T \nabla L(\boldsymbol{\rho}_i)}{\mathbf{d}_i^T \nabla^2 L(\boldsymbol{\rho}_i) \mathbf{d}_i}, \quad (66)$$

which corresponds to the step size bound in the ILS with $\epsilon_L = 0$. However, we require $\epsilon_L > 0$ to perform ILS effectively. Thus, $\mathbf{d}_i \rightarrow \mathbf{0}$ or $v_i \rightarrow 0$ are necessary for $\Delta L(\boldsymbol{\rho}_{i+1}) \rightarrow 0$. ■

APPENDIX B PROOF OF THEOREM 1

In light of (46), (48) and (65), the ILS condition requires

$$\begin{aligned} v_i \mathbf{d}_i^T \nabla L(\boldsymbol{\rho}_i) + v_i^2 / 2 \mathbf{d}_i^T \nabla^2 L(\boldsymbol{\rho}_i) \mathbf{d}_i &\leq \epsilon_L v_i \mathbf{d}_i^T \nabla L(\boldsymbol{\rho}_i) \\ \implies v_i &\leq \frac{2(\epsilon_L - 1) \mathbf{d}_i^T \nabla L(\boldsymbol{\rho}_i)}{\mathbf{d}_i^T \nabla^2 L(\boldsymbol{\rho}_i) \mathbf{d}_i}. \end{aligned} \quad (67)$$

Where positive $\mathbf{d}_i^T \nabla^2 L(\boldsymbol{\rho}_i) \mathbf{d}_i$ is considered. Assuming the Lipschitz gradient continuity of $L(\boldsymbol{\rho})$, $\|\nabla^2 L(\boldsymbol{\rho}_i)\|$ is upper bounded, indicating a positive and finite $\mathbf{d}_i^T \nabla^2 L(\boldsymbol{\rho}_i) \mathbf{d}_i$ and thus non-zero v_i . Furthermore, in light of (48), we have,

$$\Delta^2 L(\boldsymbol{\rho}_{i+1}) \leq \epsilon_L^2 v_i^2 (\mathbf{d}_i^T \nabla L(\boldsymbol{\rho}_i))^2. \quad (68)$$

Since $L(\boldsymbol{\rho})$ is a monotonously decreasing and bounded function regarding $\boldsymbol{\rho}_i$, we have $\Delta^2 L(\boldsymbol{\rho}_{i+1}) \rightarrow 0$ when $i > I$ for a large constant I . The deflection factor computed by (45) or the descent direction vector in (53) can guarantee the strict descent $\mathbf{d}_i^T \nabla L(\boldsymbol{\rho}_i) < 0$ at each iteration i unless $\mathbf{d}_i = \mathbf{0}$. Consequently, sequence $\{L(\boldsymbol{\rho}_i)\}$ will converge to a stationary point with a zero descent direction $\mathbf{d}_i \rightarrow \mathbf{0}$ when it has Lipschitz gradient continuity. According to **Lemma 1**, we have $\|\Delta\boldsymbol{\rho}_{i+1}\| \rightarrow 0$ when $\mathbf{d}_i \rightarrow \mathbf{0}$. On the other hand, we assume the objective function is not Lipschitz gradient continuous. In this case, if the sequence $\{\boldsymbol{\rho}_i\}$ pass a Lipschitz noncontinuous point $\boldsymbol{\rho}_I$ where $\mathbf{d}_I^T \nabla^2 L(\boldsymbol{\rho}_I) \mathbf{d}_I$ is extremely large, to satisfy (67), the step size should meet $v_I \rightarrow 0$. According to **Lemma 1**, we have $\|\Delta\boldsymbol{\rho}_{i+1}\| \rightarrow 0$ and $\Delta L(\boldsymbol{\rho}_{i+1}) \rightarrow 0$ when $v_i \rightarrow 0$ for $i \geq I$, i.e., the sequences $\{\boldsymbol{\rho}_i\}$ and $\{L(\boldsymbol{\rho}_i)\}$ converge to a Lipschitz gradient noncontinuous point. ■

REFERENCES

- [1] X. Pang, S. Guo, J. Tang, N. Zhao, and N. Al-Dhahir, "Dynamic ISAC beamforming design for UAV-enabled vehicular networks," *IEEE Trans. Wireless Commun.*, vol. 23, no. 11, pp. 16 852–16 864, 2024.
- [2] F. Liu, Y. Cui, C. Masouros, J. Xu, T. X. Han, Y. C. Eldar, and S. Buzzi, "Integrated sensing and communications: Toward dual-functional wireless networks for 6G and beyond," *IEEE J. Sel. Areas Commun.*, vol. 40, no. 6, pp. 1728–1767, 2022.
- [3] A. Liu, Z. Huang, M. Li, Y. Wan, W. Li, T. X. Han, C. Liu, R. Du, D. K. P. Tan, J. Lu, Y. Shen, F. Colone, and K. Chetty, "A survey on fundamental limits of integrated sensing and communication," *IEEE Commun. Surveys & Tutorials*, vol. 24, no. 2, pp. 994–1034, 2022.
- [4] Y. Xiong, F. Liu, Y. Cui, W. Yuan, T. X. Han, and G. Caire, "On the fundamental tradeoff of integrated sensing and communications under Gaussian channels," *IEEE Trans. Inf. Theory*, vol. 69, no. 9, pp. 5723–5751, 2023.
- [5] F. Liu, C. Masouros, A. Li, H. Sun, and L. Hanzo, "MU-MIMO communications with MIMO radar: From co-existence to joint transmission," *IEEE Trans. Wireless Commun.*, vol. 17, no. 4, pp. 2755–2770, 2018.
- [6] C. B. Barneto, S. D. Liyanaarachchi, M. Heino, T. Riihonen, and M. Valkama, "Full duplex radio/radar technology: The enabler for advanced joint communication and sensing," *IEEE Wireless Commun.*, vol. 28, no. 1, pp. 82–88, 2021.
- [7] N. González-Prelcic, M. Furkan Keskin, O. Kaltiokallio, M. Valkama, D. Dardari, X. Shen, Y. Shen, M. Bayraktar, and H. Wymeersch, "The integrated sensing and communication revolution for 6G: Vision, techniques, and applications," *Proc. IEEE*, vol. 112, no. 7, pp. 676–723, 2024.
- [8] A. M. Haimovich, R. S. Blum, and L. J. Cimini, "MIMO radar with widely separated antennas," *IEEE Signal Process. Mag.*, vol. 25, no. 1, pp. 116–129, 2008.
- [9] Z. Behdad, O. T. Demir, K. W. Sung, E. Björnson, and C. Cavdar, "Power allocation for joint communication and sensing in cell-free massive MIMO," in *GLOBECOM 2022-2022 IEEE Global Commun. Conf.*, 2022, pp. 4081–4086.

- [10] —, “Multi-static target detection and power allocation for integrated sensing and communication in cell-free massive MIMO,” *IEEE Trans. Wireless Commun.*, pp. 1–1, 2024.
- [11] Y. Huang, Y. Fang, X. Li, and J. Xu, “Coordinated power control for network integrated sensing and communication,” *IEEE Trans. Veh. Technol.*, vol. 71, no. 12, pp. 13 361–13 365, 2022.
- [12] A. Ahmed, Y. D. Zhang, and B. Himed, “Distributed dual-function radar-communication MIMO system with optimized resource allocation,” in *2019 IEEE Radar Conf. (RadarConf)*, 2019, pp. 1–5.
- [13] A. Ahmed and Y. D. Zhang, “Optimized resource allocation for distributed joint radar-communication system,” *IEEE Trans. Veh. Technol.*, vol. 73, no. 3, pp. 3872–3885, 2024.
- [14] W. Mao, Y. Lu, C.-Y. Chi, B. Ai, Z. Zhong, and Z. Ding, “Communication-sensing region for cell-free massive MIMO ISAC systems,” *IEEE Trans. Wireless Commun.*, vol. 23, no. 9, pp. 12 396–12 411, 2024.
- [15] A. Tajer, G. H. Jajamovich, X. Wang, and G. V. Moustakides, “Optimal joint target detection and parameter estimation by MIMO radar,” *IEEE J. Sel. Topics Signal Process.*, vol. 4, no. 1, pp. 127–145, 2010.
- [16] Y. Fang, S. Zhu, B. Liao, X. Li, and G. Liao, “Target localization with bistatic MIMO and FDA-MIMO dual-mode radar,” *IEEE Trans. Aerosp. Electron. Syst.*, vol. 60, no. 1, pp. 952–964, 2024.
- [17] J. An, H. Li, D. W. K. Ng, and C. Yuen, “Fundamental detection probability vs. achievable rate tradeoff in integrated sensing and communication systems,” *IEEE Trans. Wireless Commun.*, vol. 22, no. 12, pp. 9835–9853, 2023.
- [18] S. Dwivedi, P. Aggarwal, and A. K. Jagannatham, “Fast block LMS and RLS-based parameter estimation and two-dimensional imaging in monostatic MIMO radar systems with multiple mobile targets,” *IEEE Trans. Signal Process.*, vol. 66, no. 7, pp. 1775–1790, 2018.
- [19] Q. Qi, X. Chen, A. Khalili, C. Zhong, Z. Zhang, and D. W. K. Ng, “Integrating sensing, computing, and communication in 6G wireless networks: Design and optimization,” *IEEE Trans. Commun.*, vol. 70, no. 9, pp. 6212–6227, 2022.
- [20] M. Dianat, M. R. Taban, J. Dianat, and V. Sedighi, “Target localization using least squares estimation for MIMO radars with widely separated antennas,” *IEEE Trans. Aerosp. Electron. Syst.*, vol. 49, no. 4, pp. 2730–2741, 2013.
- [21] C.-H. Park and J.-H. Chang, “Closed-form localization for distributed MIMO radar systems using time delay measurements,” *IEEE Trans. Wireless Commun.*, vol. 15, no. 2, pp. 1480–1490, 2016.
- [22] Z. Chen, J. Tang, L. Huang, Z.-Q. He, K.-K. Wong, and J. Wang, “Robust target positioning for reconfigurable intelligent surface assisted MIMO radar systems,” *IEEE Trans. Veh. Technol.*, vol. 72, no. 11, pp. 15 098–15 102, 2023.
- [23] Q. He, R. S. Blum, H. Godrich, and A. M. Haimovich, “Target velocity estimation and antenna placement for MIMO radar with widely separated antennas,” *IEEE J. Sel. Topics Signal Process.*, vol. 4, no. 1, pp. 79–100, 2010.
- [24] M. Wang, X. Li, L. Gao, Z. Sun, G. Cui, and T. S. Yeo, “Signal accumulation method for high-speed maneuvering target detection using airborne coherent MIMO radar,” *IEEE Trans. Signal Process.*, vol. 71, pp. 2336–2351, 2023.
- [25] R. Boyer, “Performance bounds and angular resolution limit for the moving colocated MIMO radar,” *IEEE Trans. Signal Process.*, vol. 59, no. 4, pp. 1539–1552, 2011.
- [26] B. Liao, “Fast angle estimation for MIMO radar with nonorthogonal waveforms,” *IEEE Trans. Aerosp. Electron. Syst.*, vol. 54, no. 4, pp. 2091–2096, 2018.
- [27] C. Ouyang, Y. Liu, H. Yang, and N. Al-Dahir, “Integrated sensing and communications: A mutual information-based framework,” *IEEE Commun. Mag.*, vol. 61, no. 5, pp. 26–32, 2023.
- [28] M. Al-Jarrah, E. Alsusa, and C. Masouros, “A unified performance framework for integrated sensing-communications based on KL-divergence,” *IEEE Trans. Wireless Commun.*, vol. 22, no. 12, pp. 9390–9411, 2023.
- [29] H. A. Ammar, R. Adve, S. Shahbazpanahi, G. Boudreau, and K. V. Srinivas, “Downlink resource allocation in multiuser cell-free MIMO networks with user-centric clustering,” *IEEE Trans. Wireless Commun.*, vol. 21, no. 3, pp. 1482–1497, 2022.
- [30] H. Q. Ngo, A. Ashikhmin, H. Yang, E. G. Larsson, and T. L. Marzetta, “Cell-free massive MIMO versus small cells,” *IEEE Trans. Wireless Commun.*, vol. 16, no. 3, pp. 1834–1850, 2017.
- [31] X. Gan, C. Huang, Z. Yang, X. Chen, J. He, Z. Zhang, C. Yuen, Y. Liang Guan, and M. Debbah, “Coverage and rate analysis for integrated sensing and communication networks,” *IEEE J. Sel. Areas Commun.*, vol. 42, no. 9, pp. 2213–2227, 2024.
- [32] Y. Yang and R. S. Blum, “MIMO radar waveform design based on mutual information and minimum mean-square error estimation,” *IEEE Trans. Aerosp. Electron. Syst.*, vol. 43, no. 1, pp. 330–343, 2007.
- [33] G. Sun, Z. He, J. Tong, X. Yu, and S. Shi, “Mutual information-based waveform design for MIMO radar space-time adaptive processing,” *IEEE Trans. Geosci. Remote Sens.*, vol. 59, no. 4, pp. 2909–2921, 2021.
- [34] Q. He, R. S. Blum, and A. M. Haimovich, “Noncoherent MIMO radar for location and velocity estimation: More antennas means better performance,” *IEEE Trans. Signal Process.*, vol. 58, no. 7, pp. 3661–3680, 2010.
- [35] C. Wei, Q. He, and R. S. Blum, “Cramer-rao bound for joint location and velocity estimation in multi-target non-coherent MIMO radars,” in *2010 44th Ann. Conf. Inform. Sci. and Syst. (CISS)*, 2010, pp. 1–6.
- [36] Q. He and R. S. Blum, “Noncoherent versus coherent MIMO radar: Performance and simplicity analysis,” *Signal Process.*, vol. 92, no. 10, pp. 2454–2463, 2012.
- [37] Q. He, J. Hu, R. S. Blum, and Y. Wu, “Generalized cramer-rao bound for joint estimation of target position and velocity for active and passive radar networks,” *IEEE Trans. Signal Process.*, vol. 64, no. 8, pp. 2078–2089, 2016.
- [38] H. Godrich, A. M. Haimovich, and R. S. Blum, “Target localization accuracy gain in MIMO radar-based systems,” *IEEE Trans. Inf. Theory*, vol. 56, no. 6, pp. 2783–2803, 2010.
- [39] Y. Ai, W. Yi, R. S. Blum, and L. Kong, “Cramer-rao lower bound for multitarget localization with noncoherent statistical MIMO radar,” in *2015 IEEE Radar Conf. (RadarCon)*, 2015, pp. 1497–1502.
- [40] H. Godrich, A. P. Petropulu, and H. V. Poor, “Power allocation strategies for target localization in distributed multiple-radar architectures,” *IEEE Trans. Signal Process.*, vol. 59, no. 7, pp. 3226–3240, 2011.
- [41] —, “Sensor selection in distributed multiple-radar architectures for localization: A knapsack problem formulation,” *IEEE Trans. Signal Process.*, vol. 60, no. 1, pp. 247–260, 2012.
- [42] G. Xia, P. Xiao, Q. Luo, B. Ji, Y. Zhang, and H. Zhou, “Cell-free MIMO-ISAC: Joint location and velocity estimation and fundamental CRLB analysis,” *arXiv preprint arXiv:2503.06766*, 2025.
- [43] H. Zhang, Y. Zhang, X. Liu, C. Ren, H. Li, and C. Sun, “Time allocation approaches for a perceptive mobile network using integration of sensing and communication,” *IEEE Trans. Wireless Commun.*, vol. 23, no. 2, pp. 1158–1169, 2024.
- [44] F. Dong, F. Liu, Y. Cui, W. Wang, K. Han, and Z. Wang, “Sensing as a service in 6G perceptive networks: A unified framework for ISAC resource allocation,” *IEEE Trans. Wireless Commun.*, vol. 22, no. 5, pp. 3522–3536, 2023.
- [45] Z. Xu and A. Petropulu, “A bandwidth efficient dual-function radar communication system based on a MIMO radar using OFDM waveforms,” *IEEE Trans. Signal Process.*, vol. 71, pp. 401–416, 2023.
- [46] F. Liu, Y.-F. Liu, A. Li, C. Masouros, and Y. C. Eldar, “Cramer-rao bound optimization for joint radar-communication beamforming,” *IEEE Trans. Signal Process.*, vol. 70, pp. 240–253, 2022.
- [47] X. Li, F. Liu, Z. Zhou, G. Zhu, S. Wang, K. Huang, and Y. Gong, “Integrated sensing, communication, and computation over-the-air: MIMO beamforming design,” *IEEE Trans. Wireless Commun.*, vol. 22, no. 8, pp. 5383–5398, 2023.
- [48] H. L. Van Trees, *Detection, estimation, and modulation theory*. John Wiley & Sons, 2001.
- [49] H.-Z. Feng, H.-W. Liu, J.-K. Yan, F.-Z. Dai, and M. Fang, “A fast efficient power allocation algorithm for target localization in cognitive distributed multiple radar systems,” *Signal Process.*, vol. 127, pp. 100–116, 2016.
- [50] E. Fishler, A. Haimovich, R. Blum, L. Cimini, D. Chizhik, and R. Valenzuela, “Spatial diversity in radars—models and detection performance,” *IEEE Trans. Signal Process.*, vol. 54, no. 3, pp. 823–838, 2006.
- [51] W. L. Melvin and J. Scheer, *Principles of modern radar. Vol. II, Advanced techniques*. Raleigh: SciTech Pub., 2013.
- [52] Q. He, N. H. Lehmann, R. S. Blum, and A. M. Haimovich, “MIMO radar moving target detection in homogeneous clutter,” *IEEE Trans. Aerosp. Electron. Syst.*, vol. 46, no. 3, pp. 1290–1301, 2010.
- [53] P. Wang, H. Li, and B. Himed, “Moving target detection using distributed MIMO radar in clutter with nonhomogeneous power,” *IEEE Trans. Signal Process.*, vol. 59, no. 10, pp. 4809–4820, 2011.
- [54] *Penalty and Barrier Functions*. John Wiley & Sons, Ltd, 2006, ch. 9, pp. 469–535.
- [55] M. R. Hestenes, E. Stiefel *et al.*, *Methods of conjugate gradients for solving linear systems*. NBS Washington, DC, 1952, vol. 49, no. 1.
- [56] *Unconstrained optimization*. John Wiley & Sons, Ltd, 2006, ch. 8, pp. 343–468.

- [57] L. Armijo, "Methods of conjugate gradients for solving linear systems," *Pacific J. Math.*, vol. 16, no. 1, pp. 1–3, 1966.
- [58] —, "Minimization of functions having lipschitz continuous first partial derivatives." *Pacific J. Mathematics*, vol. 16, pp. 1–3, 1966.
- [59] Searcoid, Mícheál Ó, *Lipschitz Functions, Metric Space*. Springer-Verlag, 2006.
- [60] X. Ouyang and J. Zhao, "Orthogonal chirp division multiplexing," *IEEE Trans. Commun.*, vol. 64, no. 9, pp. 3946–3957, 2016.